



High-robustness intravascular photoacoustic endoscope with a hermetically sealed opto-sono capsule

XUE WEN,^{1,2}  **PENG LEI,^{1,2}** **KEDI XIONG,^{1,2}** **PENGFEEI ZHANG,^{3,4,5}**
AND SIHUA YANG^{1,2,6}

¹*MOE Key Laboratory of Laser Life Science & Institute of Laser Life Science, College of Biophotonics, South China Normal University, Guangzhou 510631, China*

²*Guangdong Provincial Key Laboratory of Laser Life Science, College of Biophotonics, South China Normal University, Guangzhou 510631, China*

³*Department of Cardiology, Qilu Hospital, Cheeloo College of Medicine, Shandong University. NO.107 Wenhua Road, Jinan, Shandong Province 250012, China*

⁴*Key Laboratory of Cardiovascular Remodeling and Function Research, Chinese Ministry of Education and Chinese National Health Commission Shandong University, Jinan 250100, China*

⁵*pengf-zhang@163.com*

⁶*yangsh@scnu.edu.cn*

Abstract: The prevailing open-structure intravascular photoacoustic (IVPA) endoscope emits a gradually deformed laser beam with exposed optical or acoustical components bearing pollution and damage in arterial lumen. Deformed laser beam scanning, which causes a low excitation efficiency and serious deterioration of the transverse resolution, is a current big obstacle to the application of photoacoustic endoscopy in intravascular imaging. Hence, the stable and reliable IVPA endoscope is indispensable. In this letter, we designed a high-robustness intravascular photoacoustic (HR-IVPA) endoscope with a hermetically sealed opto-sono capsule. The distal end of the opto-sono capsule was integrated with miniaturized optics, including a customized C-Lens and a customized total-reflection prism (TRP). The TRP was first applied to a side-viewing IVPA endoscope, featuring a high-throughput energy coupling efficiency of 90% and a cut-off free damage threshold. The optical path structure of the endoscope, optimized using optical simulation tools, overcame the ambiguous focus shift caused by chromatic dispersion and achieved a waist size of 20 μm as well as a focus depth of 4 mm in water at the wavelength of 1200 nm. The mass phantom experiments demonstrated that the HR-IVPA endoscope afforded repeatable IVPA images with a relatively constant signal-to-noise ratio (SNR) of about ~ 41.8 dB and a transverse resolution of about ~ 23 μm . The imaging experiments of the stent and lipid further demonstrated the robustness and validated the imaging ability of the HR-IVPA endoscope, which opens a new avenue for improving the endoscopic imaging capability, strengthening the credible detection of atherosclerotic cardiovascular disease.

© 2020 Optical Society of America under the terms of the [OSA Open Access Publishing Agreement](#)

1. Introduction

Atherosclerotic cardiovascular disease (ASCVD) is the leading cause of death with high morbidity and mortality worldwide [1]. Endovascular imaging based on various principles have been proposed successively for ASCVD diagnosis. Intravascular ultrasound imaging (IVUS) can provide reliable vascular morphological information, including vessel structure and lumen geometry. However, the specificity and sensitivity recognition of lipid-rich plaques is limited [2]. Intravascular optical coherence tomography (IVOCT) has a higher spatial resolution than IVUS, which can be used to detect the thickness of fiber caps and disruption of the intima. However, the imaging depth is relatively low [3,4]. Intravascular photoacoustic (IVPA) imaging is rapidly emerging as a novel imaging technology, which can provide structure, function, and

molecular information of biological tissues [5–21]. Taking the advantage of diffusive photons, IVPA imaging makes a specialty of providing volumetric images of tissues with high optical contrast and high ultrasonic spatial resolution at sufficient imaging depths [22,23]. Moreover, the IVPA imaging with a 1200 nm or 1720 nm excitation light source can quantitatively and reliably define the plaque lipid core by extracting lipid concentration and morphological distribution information [24–26].

Clinically ideal photoacoustic endoscopic catheters should have the characteristics of small size, high resolution, high sensitivity, and deep-penetration imaging depth. In recent years, in order to optimize the imaging indexes mentioned above, novel device units and reasonable structural designs for IVPA imaging catheters have been proposed by various research groups [27–28]. The Emelianov group reported two IVPA imaging catheter structures based on side-view fiber and front-surface mirror (FSM), respectively, with optics and ultrasonic transducers presenting a sequence arrangement on the axis [27]. The Chen group proposed an IVPA imaging catheter structure with side-view fiber and ultrasound transducer set in parallel. An ultrasound transducer with a frequency of 80 MHz was applied for the first time to obtain a significant axial resolution of 35 μm [28]. The Cheng team proposed a collinear structure design that an ultrasonic transducer was placed parallel to the side-view fiber, with its sensing area facing the 45° polished bevel. Ultrasound was reflected twice through the FSM and polished bevel, received by the ultrasonic transducer. The novel optical and acoustic collinear design aims to improve imaging sensitivity [29]. The Song team optimized the diameter of the IVPA imaging catheter from 1.1 mm to 0.9 mm by carefully integrating the spatial layout of the device units in the IVPA imaging catheter [30,31]. The IVPA imaging catheter based on tapered fiber proposed by our team cleverly combined the characteristics of high-energy coupling of large-core fiber and high-quality spot outputted from small-core fiber to achieve a deep-penetration imaging from intima to adventitia [32]. Despite these advances, side-view fiber or FSM is inevitably used in IVPA endoscopes for side-view scanning. The IVPA endoscope based on side-view fiber is a relatively closed structure, sacrificing the high-resolution of focal beam. Meanwhile, the large-spot illumination reduces the exciting efficiency. Although the FSM-based endoscopes can be flexibly equipped with focusing lens to realize optical-resolution IVPA imaging, these structures are partially exposed to the blood environment, which results in the oxidative corrosion and damage of optical units [33]. The open-structure IVPA endoscope deteriorates the imaging quality in several experiments. Hence, researches on high-robustness IVPA endoscope with hermetically closed structure for stable and reliable IVPA imaging deserves widespread attention.

In the clinical setting, the intervention procedure of imaging catheter is usually accompanied with saline or contrast flush to improve the imaging quality. However, the saline flush is an intermittent process. Frequent or long-lasting saline flush will increase the risk of myocardial ischemia. In addition, the structure of the sheath is not enclosed with a tiny hole opened in the catheter tip [34]. The stagnation of the imaging catheter in the lumen will lead to an inevitable backflow of blood into the catheter, which may pose a threat to the stability of optical or opto-sono endoscopes.

In this study, we proposed an improved endoscopic structure with hermetically sealed opto-sono capsule for highly repeatable IVPA imaging in arterial lumen. In this endoscope, a laser beam was delivered through a single-mode fiber (SMF), focused by a C-Lens and eventually reflected by a total-reflection prism (TRP). The air gap of the opto-sono capsule was filled with index-matching optical glue for all solid seal and total reflection. It owns several advantages: (1) the hermetically sealed optical cavity is isolated from the external environment, which brings it long service life and stable optical excitation for IVPA imaging in blood environment; (2) the side-viewing endoscope based on TRP features a high-throughput energy coupling efficiency and a cut-off free damage threshold, which leads to a high photoacoustic excitation efficiency; (3) the customizable optical-resolution focus ensures the high SNR and transverse resolution with expected imaging

depth. Then this new opto-sono endoscope was used to our lab-built IVPA imaging system and evaluated its performance with phantom experiments [32].

2. Methods and materials

2.1. Structural design of HR-IVPA endoscope

The structural design of the HR-IVPA endoscope is shown in Fig. 1. The laser beam emitted from the single-mode fiber (SMF) (PM-TSF-9/125, Nufern, USA) is focused by the C-Lens (customized, Fuzhou Gongxin Photoelectric Technology Co., Ltd., Fujian, China) and reflected by the TRP (customized, Nanyang Jingliang Photoelectric Co., Ltd., Henan, China). The electrical wire is embedded at the bottom of the metal house, placed in a torsion coil in parallel with a SMF. The torsion coil (customized, Asahi Intecc, Aichi, Japan) is docked with the tail end of the metal house (customized, Cloud Engineering Industrial Technology Co., Ltd., China). Figures 1(a) and 1(b) show the structure of HR-IVPA endoscope before and after assembly. Figure 1(d) shows the micrograph of the fabricated HR-IVPA endoscope. The reflective bevel of TRP is polished to 35° , achieving a 55° angle of incidence. According to the critical angle formula for total reflection: $\theta_c = \arcsin(n_2/n_1)$, where $\theta_c=51.3^\circ$ is the critical angle, n_2 represents the refractive index of optical glue, n_1 represents the refractive index of optical glass. The air gap of HR-IVPA endoscope is filled with optical glue (Epotek 310M, Epoxy Technology Co., Ltd., USA), with a light transmittance of over 99% in the wavelength range of 400-1300 nm and over 90% in 1400-2200 nm, solidifying at room temperature for 24 hours [35]. The glass-glue bevel achieves a total-reflection surface for the conditions of total reflection that the incident angle is greater than the critical angle and the laser beam propagates from the light-dense medium to the light-sparse medium. The curved surface of the cylindrical TRP was polished to a flat surface, which emits laser beam as window, to avoid the astigmatism effect of beam spot. The polishing depth is 0.07 mm, keeping a slit width of 300 μm bar-shaped light window. The laser beam reflected by TRP finally emits from the light window, with the optical focus formed above the ultrasonic transducer (customized, Suzhou Institute of Biomedical Engineering and Technology, Chinese Academy of Sciences, Suzhou, China). The rigid length of the catheter tip is about ~5 mm and the diameter of the endoscope is 1 mm. Figure 1(c) describes the working principle of HR-IVPA endoscope, and the upper left inset explains the hermetically sealed design and the principle of TRP. Structurally, the rigid opto-sono capsule with all-solid-state cavity can alleviate the mechanical vibration and ensure the collaborative operation between the optical components. Besides, the hermetically sealed optical cavity is isolated from the outside environment to avoid the interference.

2.2. Optical simulation of HR-IVPA endoscope

The assembly was conducted in the air, using a guiding light with a wavelength of 637 nm. However, for the IVPA imaging of lipid-rich plaque, pulsed laser with a wavelength of 1200 nm or 1720 nm is often applied. Moreover, water is essential as a coupling agent for ultrasound. From assembly to experiment, chromatic aberration is introduced by variation in light wavelength and coupling medium and the focus shift becomes ambiguous, which lead to inaccurate optical-resolution IVPA imaging.

In order to quantify the optical-resolution focus, the ZEMAX software was used for optical simulation. The simulated laser beam focused by C-Lens under assembly conditions (C_0 : laser in air, at 637 nm) and experimental conditions (C_2 : laser in water, at 1200 nm; C_3 : laser in water, at 1720 nm) are shown in Fig. 2(a). With an equal length (L) between the SMF and C-Lens, it can be inferred that the focus length under experimental conditions satisfy the equation: $FL = F_0 + P_0 + P_{11}(P_{12})$, where FL is the required parameter of focus length, F_0 is a fixed focal length under the conditions of C_0 , P_0 is the focus shift caused by the change of coupling

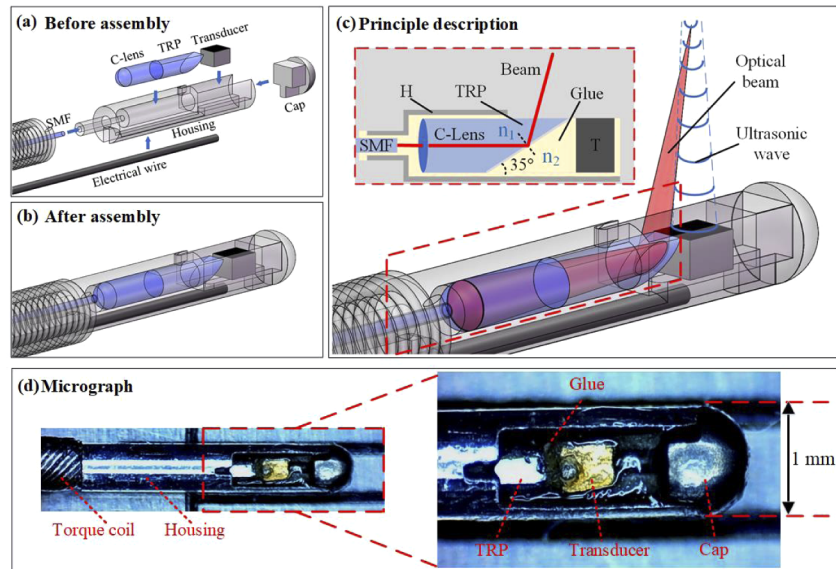


Fig. 1. Design and assembly of the HR-IVPA endoscope with hermetically sealed opto-sono capsule. (a) The schematic of main components before assembly. (b) The schematic of assembled HR-IVPA endoscope. (c) Zoom-in view of the probe tip with emitted laser and excited ultrasonic waves. The upper left inset is the description of how the total-reflection prism works and endoscope is solidified. Optical glass (ZF14) and optical glue (Epotek 310M) with a refractive index of n_1 and n_2 (Nd: $n_1=1.9176$, $n_2=1.497$) matches the conditions of total reflection. (d) Photograph of the fabricated HR-IVPA endoscope. T, transducer; H, housing; TRP, total-reflection prism; SMF, single mode fiber.

medium, P_{11} is the focus shift due to the change in wavelength from 637 nm to 1200 nm, P_{12} is the focus shift due to the change in wavelength from 637 nm to 1720 nm. For IVPA imaging of lipid-rich plaque, a laser beam with narrow beam waist and proper focal length is desired for high-resolution and deep-penetration IVPA imaging [32]. Figures 2(b) and 2(c) show the simulated focus length and waist, defined as the full width at half maximum (FWHM) of laser beam, as a function of the distance L . Drawing conclusions by combining the simulation results of Figs. 2(b) and 2(c), an optimized laser beam appears when the distance L is controlled at 1.3 mm. For the equal distance L , the FWHM at waist is $16.4 \mu\text{m}$ and the focal length is 4.08 mm under the conditions of C_2 . Under the conditions of C_0 , the FWHM at waist is $14.4 \mu\text{m}$ and the focal length is 2.59 mm. It should be noted that there is an invalid focus length of 1 mm due to the inherent length of TRP. By referring to the assembly parameters under the condition of C_0 , assembly work was conducted to indirectly acquire the ideal optical-resolution endoscopes suitable for the experimental conditions.

2.3. Light field measurement of HR-IVPA endoscope

To verify the simulation results, the beam profile under the conditions of C_2 was measured at different distances (0-8 mm) using a lab-built three-dimensional (3D) light field scanning system. The architecture of the 3D light field scanning system is shown in the Fig. 3(a). Optical excitation via an optical parametric oscillator (OPO) (NT200 Series Laser, Ekspla, Vilnius, Lithuania) outputted laser beam at a wavelength of 1200 nm and a repetition rate of 2.5kHz. The output laser was spatially attenuated and reshaped, and focused into the SMF by an objective lens (RMS4X, Thorlabs, New Jersey, USA). The distal end of the endoscopic catheter was fixed on

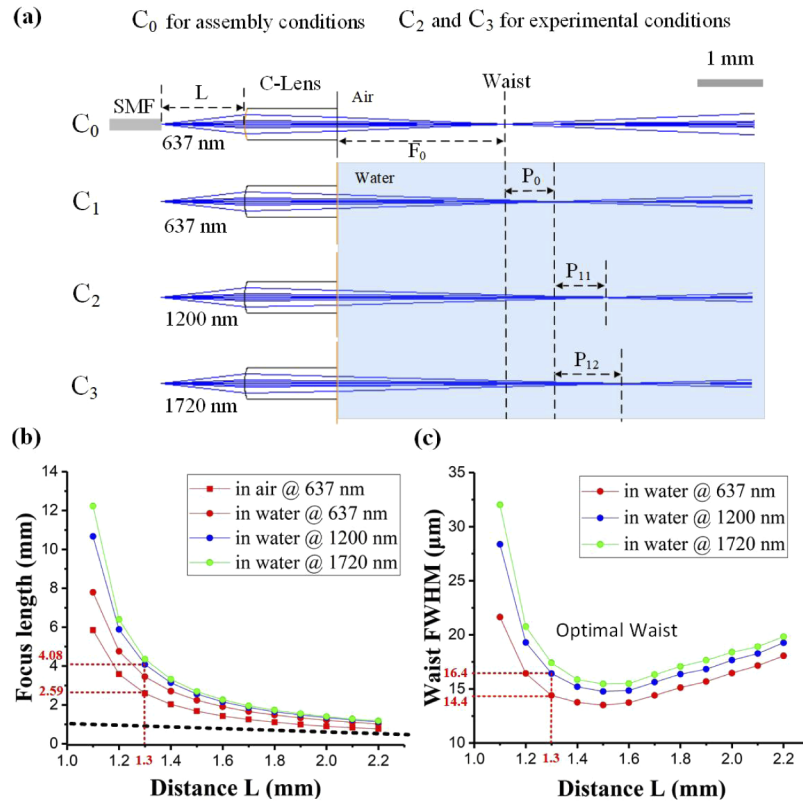


Fig. 2. Optical simulation of HR-IVPA endoscope. (a) The simulated laser beam focused by C-Lens under assembly and experimental conditions. L represents the interval between SMF and C-Lens; F_0 represents the focus length under the conditions C_0 ; P_0 , P_{11} and P_{12} represent the focus shift. (b) The simulated focus length as a function of the distance L . (c) The simulated waist' FWHM as a function of the distance L .

the Z stepping stage, controlled by a field-programmable gate array (FPGA) with 20 μm step size. A spot analyzer (CMOS-1202, Cinogy, Germany), with a response wavelength range of 150 nm~1605 nm, was fixed on the X-Y manual displacement platform and connected to the personal computer (PC) to achieve synchronous acquisition of tomographic images of laser beam. It should be noted that the spot analyzer is sensitive to a limited range of laser wavelengths. Therefore, the laser at the wavelength of 1720 nm has not been measured. Plastic wrap was used for waterproof treatment to the spot analyzer and standard deionized water was used as the optical coupling medium. The light field was measured in water at the wavelength of 1200 nm and the VOLVIEW software was employed to process the tomographic images. The 3D reconstructed light field is shown in the Fig. 3(b). Two cross sections were picked at the distance of 2 mm (D_1) and 4 mm (D_2) as a reference to compare the simulated and measured results. Simulated and measured images of spot profile are shown in Fig. 3(d). The FWHM of the beam profile at the distance of D_1 was 36 μm in measurement and 35.45 μm in simulation. The FWHM of the beam profile at the distance of D_2 was 20 μm in measurement and 16.42 μm in simulation. The simulation and measurement of two similar curves on beam's FWHM along the beam axis (0-6 mm) is shown in Fig. 3(c). The focus was located at the distance about ~4 mm as expected by the simulation results in Fig. 2(b).

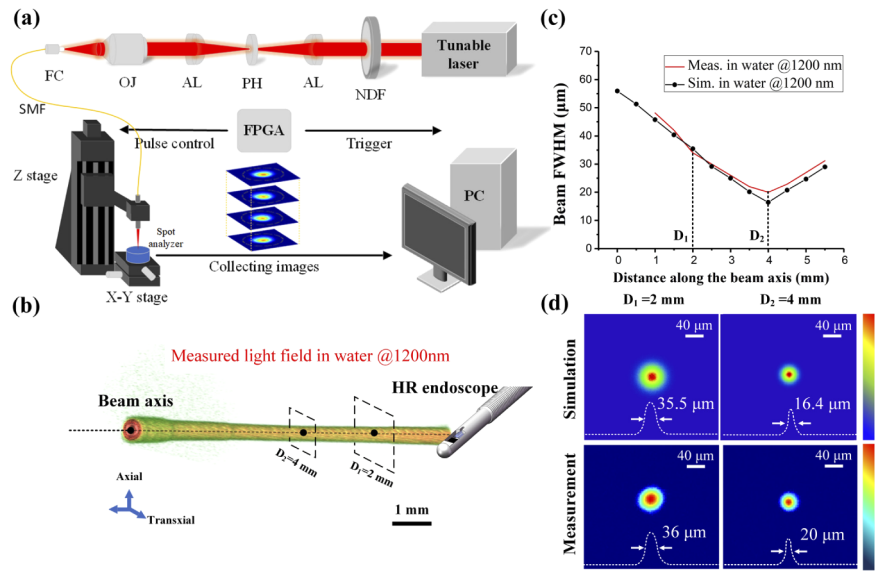


Fig. 3. Light field measurement of HR-IVPA endoscope. (a) Architecture of the 3D light field scanning system. (b) 3D reconstruction of the measured light field emitted from HR-IVPA endoscope. (c) The simulation and measurement of beam's FWHM along the beam axis. (d) The simulation and measurement of spot profile at the emission distance of 2 mm and 4 mm. SMF, single-mode fiber; FC, fiber collimator; OJ, objective; AL, aspherical lens; NDF, neutral density filter; PC, personal computer; D_1 , Distance₁; D_2 , Distance₂;

2.4. Preparation for the experiments

A phantom, with the 10 μm diameter tungsten wires distributed in holes 1~7, was made for IVPA imaging experiments in section 3.1. There was 45° angle and 0.5 mm equidistance between each hole in the direction of the longitudinal axis. The phantom was made by the following steps: (1) the lid and bottom plate were 3D printed with corresponding tiny hole; (2) the tungsten wires were threaded through two holes and fixed with glue; (3) the blood-water mixture was injected into the mold for opto-sono coupling. Mass PA imaging experiments on the phantom were conducted 3 hours a day for 6 consecutive days. The output energy of the endoscopes was controlled at 3 μJ /pulse. Anticoagulant-containing blood and water were mixed in a ratio of 1:3 as coupling medium for acoustic and optical coupling. The endoscopes were ultrasonically cleaned after each experiment, and then stored dust-free in air for the next experiment. 3000 Aline per B-scan was acquired to perform the transvers resolution in the phantom experiment, which results in a rotation speed of 0.83 revolutions per second (RPS) to acquire the data. The same experimental setting was used for the imaging experiments of imitated stent and lipid.

In the experiments of comparing the energy coupling efficiency and damage threshold of the two types of IVPA endoscopes, described in section 3.1, the TRP-based endoscopes and FSM-based endoscopes were assembled with three samples numbered 1-3 separately. Among these, No. 1 and No. 2 were assembled with SMF and No. 3 were assembled with multi-mode fiber (MMF). Laser with a wavelength of 1720 nm was delivered into the endoscopes for optical power detection. By controlling constant input energy of 3 μJ and adjusting the space coupling, the maximum (MAX) output energy was recorded. Subsequently, by increasing the input energy, the damage threshold was recorded when output energy plunged, accompanied with the laser damaged optical components.

In addition, a confirmatory experiment was done to explain the deteriorated performance of FSM-based endoscopes and high-performance of TRP-based endoscopes in IVPA imaging, shown as Figs. 5(f) and 5(g). The experimental steps are as follows: (1) FSM and TRP with good degree of finish were selected and photographed under the microscope; (2) the mixture with 0.9% saline and blood was prepared to imitate the clinical setting; (3) the selected FSM and TRP were soaked in the mixture for 3 hours at room temperature; (4) the FSM and TRP were taken out and photographed under the microscope;

During the IVPA imaging experiments of imitated stent and lipid described in sections 3.2 and 3.3. The imitated stent with a diameter of about ~4 mm was customized, whose wire width is 150 μ m. Fresh pork fat was frozen, cut into pieces and buried in agar for IVPA imaging. 1:5 blood-saline mixture was prepared for coupling agent in both IVPA imaging experiments. The HR-IVPA endoscope was used to perform 3D-scanning imaging of the lipid and imitated stent with 30 μ m step size. The output laser energy from the endoscopes is limited below ~5 μ J per pulse at the wavelength of 1720 nm, corresponding to a fluence of ~400 mJ/cm² per pulse at the tissue surface (assuring the optical focus is 1 mm below tissue), which is far below the 1 J/cm² maximum permissible exposure(MPE) safety standard of the American National Standard Institute (ANSI) safety standard [36].

3. Results

3.1. Robustness evaluation of the TRP-based and FSM-based endoscopes

To demonstrate the robustness of the HR-IVPA endoscope in IVPA imaging. A phantom was designed for the IVPA imaging experiments. Schematic diagram of the phantom is shown in Fig. 4(c). The FSM-based IVPA endoscope, reported in our previous research, was assembled to make a comparison with the TRP-based IVPA endoscope [32]. As is shown in the Figs. 4(a) and 4(b), initially, both types of IVPA endoscope performed well with a full imaging depth of 5 mm. As time went by and usage times increased, some signals seemed to be blurry and even missing for the FSM-based IVPA endoscope. The signal-to-noise ratio (SNR) and transverse resolution, taking point 3 as a reference, was calculated to evaluate the repeatability of imaging results. As is shown in the Figs. 4(d) and 4(e), the TRP-based IVPA endoscope gained stable SNR of about ~41.8 dB and transverse resolution of about ~23 μ m, sustaining repeatable imaging results. For the FSM-based IVPA endoscope, the SNR and transverse resolution continued to deteriorate with a loss of imaging depth of 2 mm. Obviously, the TRP-based IVPA endoscope is robust than FSM-based IVPA endoscope to perform high-stability IVPA imaging. The poor axial resolution of Fig. 4(a) was attributed to the bad performance of the ultrasonic transducer. The axial resolution was improved on the sixth day, because the PA signals under low-efficiency excitation were not strong enough to increase the pulse periods of ultrasonic transducer. The statistical results of IVPA imaging for 6 consecutive days are shown in Table 1. The FSM-based IVPA endoscope had a poor performance in repeatable IVPA imaging when long-term use or repeated use occurred. In contrast, the TRP-based IVPA endoscope possessed a long service life for high-stability IVPA imaging, with stable imaging parameters, such as the SNR, transverse resolution and imaging depth.

To compare the energy coupling efficiency and damage threshold of the two types of IVPA endoscopes, both TRP-based endoscopes and FSM-based endoscopes were assembled for the test experiments. Statistical results of energy coupling efficiency and damage threshold are shown in Table 2. According to the statistics, the TRP-based IVPA endoscopes performed a 14% higher coupling efficiency than the FSM-based IVPA endoscopes on average. The FSM-based IVPA endoscopes irreparably ended with the damaged FSM with an average damage threshold of 7.37 μ J. The TRP-based IVPA endoscopes ended with the broken input end of SMF and MMF. However, the TRP-based endoscopes worked again when the damaged fiber was repaired, which demonstrated that the high-performance of TRP supported a cut-off free damage threshold.

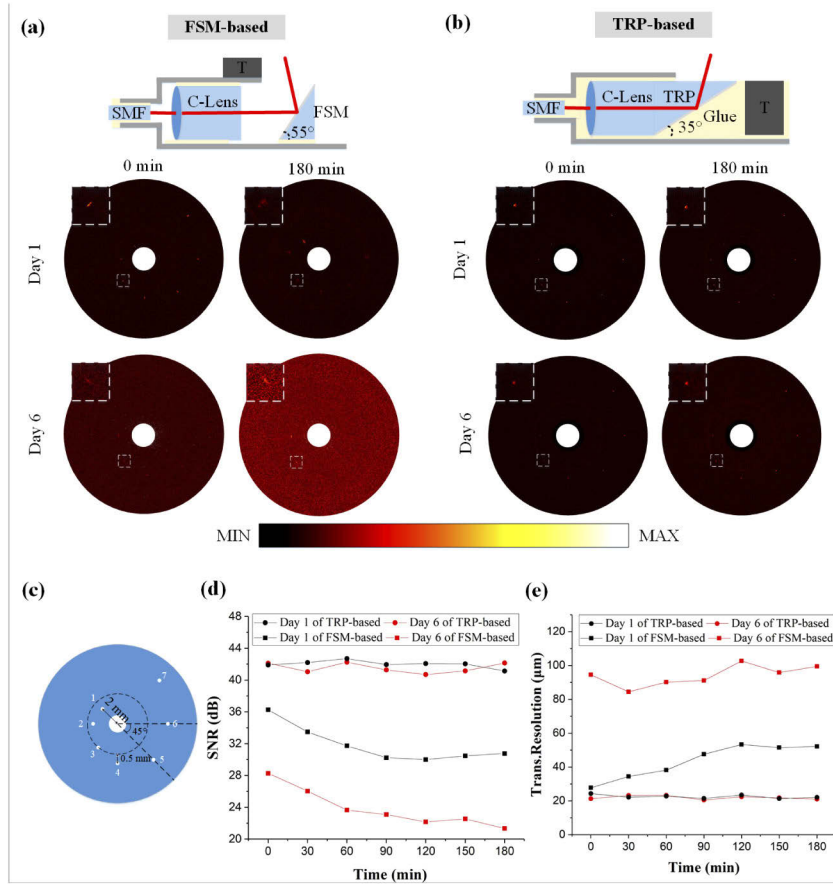


Fig. 4. Repeatability comparison of FSM-based and TRP-based IVPA endoscope. (a) The schematic diagram and deteriorated performance of FSM-based IVPA endoscope in day 1 and day 6. (b) The schematic diagram and repeatable performance of TRP-based IVPA endoscope in day 1 and day 6. (c) Schematic diagram of the phantom. (d) The SNR of PA images as a function of time. (e) The transverse resolution of PA images as a function of time. FSM, front surface mirror; TRP, total-reflection prism; T, transducer; SMF, single mode fiber.

Table 1. The statistical results of IVPA imaging for 6 consecutive days.

DAYS	FSM-based IVPA endoscope			TRP-based IVPA endoscope		
	SNR (dB)	Transverse resolution (μm)	Imaging depth (mm)	SNR (dB)	Transverse resolution (μm)	Imaging depth (mm)
1	30.7	52.16	5	41.2	22.12	5
2	27.6	63.15	4.5	38.6	21.4	5
3	25	76.5	4.5	43.7	21.91	5
4	22.8	93.3	4	39	22	5
5	22.3	109.96	3.5	45.8	22.4	5
6	21.4	95.78	3	42.2	22.45	5

Table 2. Statistical evaluation of energy coupling efficiency and damage threshold.

NO.	FSM-based IVPA endoscope				TRP-based IVPA endoscope			
	MAX output (μJ)	Coupling rate (%)	Damaged unit	Damage threshold (μJ)	MAX output (μJ)	Coupling rate (%)	Damaged unit	Damage threshold (μJ)
1	2.25	75	FSM	7	2.76	92	SMF	11
2	2.21	73.7	FSM	7.3	2.69	90	SMF	12.6
3	2.4	80	FSM	7.8	2.66	88.7	MMF	42

To demonstrate the robustness of HR-IVPA endoscope from a micro perspective, the TRP and FSM were removed from the assembled endoscopes and observed under the microscope. Figure 5(a) shows the FSM with good cleanliness, which initially performed a sound spot. Figure 5(b) shows the FSM with metal film falling off, which was caused by excessive single pulse energy of 7.3 μJ . The damaged FSM performed a breaking spot. Figure 5(c) shows the FSM with contamination, which occurred when the FSM-based endoscopes were used for two consecutive days without ultrasonic cleaning. The contaminated FSM performed a stained spot with bubble-like shadow. Figure 5(d) shows the FSM with oxidative corrosion, which was removed from the FSM-based endoscope after 6-day service life and performed a diffused spot. In comparison, the TRP was removed from the TRP-based endoscope after 6-day service life similarly, shown in the Fig. 5(e). It always performed a non-fragile spot without distortion. It can be concluded that FSM is susceptible to contamination, oxidative corrosion, and is limited by laser damage threshold. The optical performance of TRP can keep well instead. The micrograph of FSM and TRP, soaked in simulated clinical environment for 3 hours, were shown in Figs. 5(f) and 5(g). Obviously, the finish of the FSM became poor, which eventually affected the equality of laser beam. However, the finish of the TRP was still good.

3.2. High-robustness imaging and 3D reconstruction of stent

To demonstrate the robustness of HR-IVPA endoscope, the imitated stent was chosen for IVPA imaging. Figure 6(a) shows a photograph of the imitated stent sample. Figures 6(c) and 6(d) show the B-scan images of TRP-based and FSM-based endoscope at the time of 0 and 180 min, respectively. A zoom-in view of the signal spot was exemplified in the white dashed frame. To achieve a quantitative comparison of transverse resolution between the two type of endoscopes, Gaussian fitting was conducted based on the PA data extracted from the white dash line in each inset, shown as Figs. 6(e) and 6(f). The TRP-based endoscope performed a transverse resolution of 169 μm at 0 min and that of 172 μm at 180 min. However, the FSM-based endoscope performed a transverse resolution of 175 μm at 0 min and that of 218 μm at 180 min. An obvious deteriorated resolution of FSM-based endoscope was observed, compared with the repeatable imaging result of TRP-based endoscope. Experimental results demonstrated the priority of HR-IVPA endoscope in IVPA imaging of imitated stent. In addition, 3D reconstruction of the imitated stent was obtained by the HR-IVPA endoscope, shown as Fig. 6(b), to verify the imaging ability for the intravascular imitated stent.

3.3. High-robustness imaging and 3D reconstruction of a lipid

To further demonstrate the robustness and validate the imaging ability of the HR-IVPA endoscope, experiments were conducted to image a lipid by using TRP-based and FSM-based endoscope respectively, as shown in Figs. 7(c) and 7(d). Figure 7(a) shows the cross photograph of imaging mold with the fat sample. The IVPA imaging of lipid sample was obtained with a deep-penetration depth of about ~ 1.5 mm. A zoom-in view of the lipid profile was exemplified in the white dashed frame. To compare the transverse resolution of lipid images, acquired by the two types of

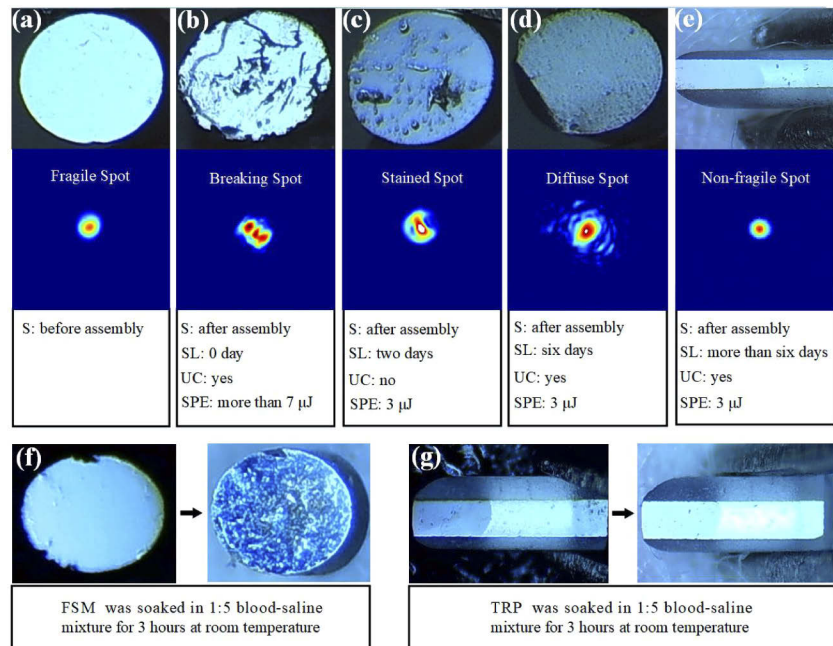


Fig. 5. The photographs of FSM and TRP, removed from assembled endoscopes with corresponding spot profiles. (a) The FSM with good cleanliness performed a fragile spot. (b) The FSM with laser damage performed a breaking spot. (c) The FSM with contamination performed a stained spot. (d) The FSM with oxidative corrosion performed a diffuse spot. (e) The high-performance TRP performed a non-fragile spot. (f) Cleanliness of FSM in a simulated clinical environment. (g) Cleanliness of FSM in a simulated clinical environment. S, state; SL, service life; UC, ultrasonic cleaning; SPE, single pulse energy; FSM, front surface mirror; TRP, total-reflection prism;

endoscope, Boltzmann fitting and differentiation were conducted based on the PA data extracted from the white dash line in each inset, shown as Figs. 7(e) and 7(f). The TRP-based endoscope performed a transverse resolution of $80\ \mu\text{m}$ at 0 min and that of $86\ \mu\text{m}$ at 180 min. However, the FSM-based endoscope performed a transverse resolution of $98\ \mu\text{m}$ at 0 min and that of $225\ \mu\text{m}$ at 180 min. An obvious deteriorated resolution of FSM-based endoscope was observed compared with the repeatable imaging result of TRP-based endoscope. Experimental results demonstrated the priority of HR-IVPA endoscope in IVPA imaging of lipid.

After verification of robustness, the HR-IVPA endoscope was used to perform 3D-scanning imaging of the lipid with $30\ \mu\text{m}$ step size and 3000 A-line per B-scan image. The in-situ distribution of bulk lipid was restored by 3D reconstruction of the PA data, shown as Fig. 7(b). The profile of the bulk lipid was clearly to be distinguished due to the high transverse resolution and SNR imaging of HR-IVPA endoscope.

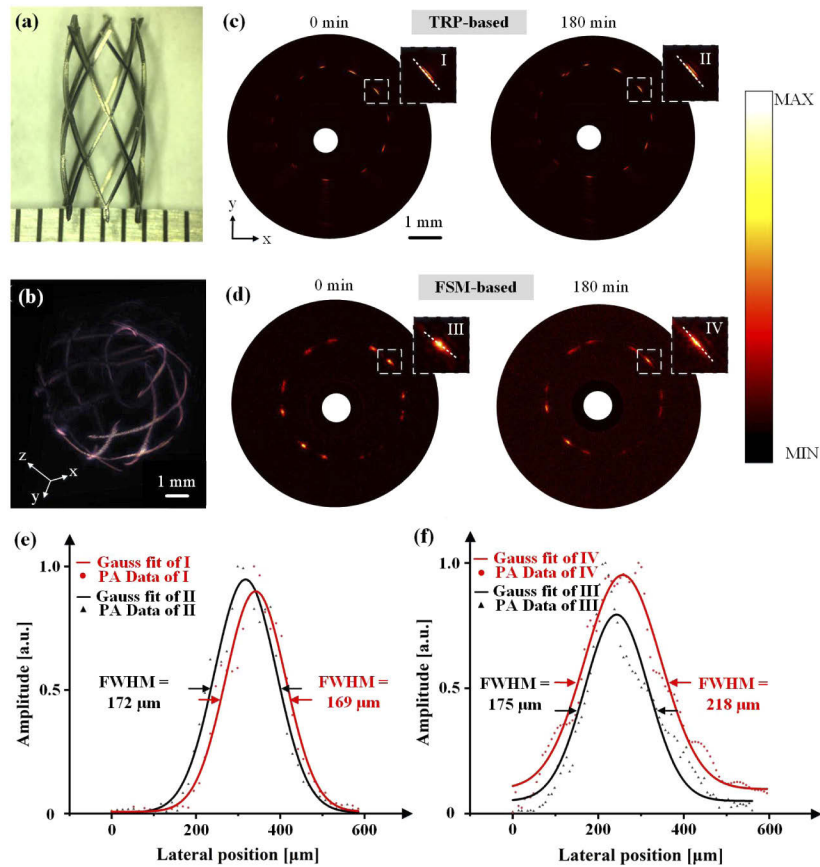


Fig. 6. Repeatability comparison of FSM-based and TRP-based endoscope on IVPA imaging of stent. (a) Photograph of stent. (b) 3D reconstruction of stent based on the data of TRP-based endoscope. (c) B-scan PA images of TRP-based endoscope at the time of 0 and 180 min with repeatable result in the inset. (d) B-scan PA images of FSM-based endoscope at the time of 0 and 180 min with deteriorated resolution in the inset. (e) Transverse resolution of TRP-based endoscope on IVPA imaging of imitated stent. (f) Transverse resolution of FSM-based endoscope on IVPA imaging of imitated stent.

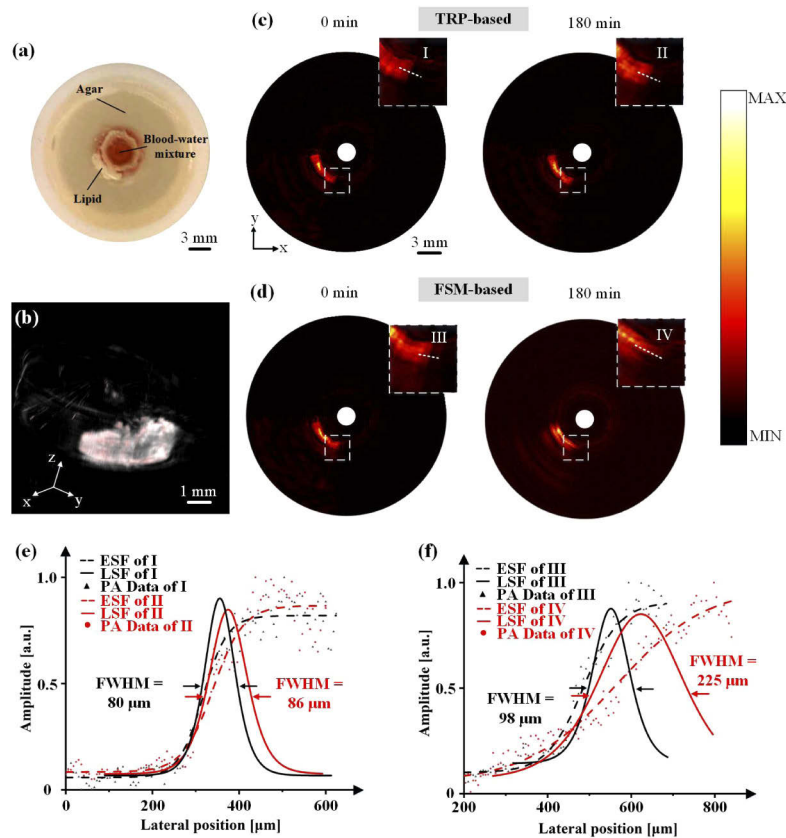


Fig. 7. Repeatability comparison of FSM-based and TRP-based endoscope on IVPA imaging of lipid. (a) Cross photograph of lipid. (b) 3D in-situ reconstruction of bulk lipid based on the data of TRP-based endoscope. (c) B-scan PA images of TRP-based endoscope at the time of 0 and 180 min with repeatable result in the inset. (d) B-scan PA images of FSM-based endoscope at the time of 0 and 180 min with deteriorated resolution in the inset. (e) Transverse resolution of TRP-based endoscope on IVPA imaging of lipid. (f) Transverse resolution of FSM-based endoscope on IVPA imaging of lipid.

4. Discussion

When the incident angle increases from light-dense medium to light-sparse medium to a certain critical angle, total reflection phenomenon occurs [37,38]. However, under the experimental conditions of water as a coupling agent, the total-reflection interface between glass and water still contains unstable factors. Impurities adhering to the outer surface of total-reflection interface will partially destroy the total-reflection conditions, resulting in leakage of the irradiated laser energy. A refractive index-matched optical glue, cooperated with optical glass, was used to form a stable total-reflection interface to solve the above problem.

The accumulated intrinsic length of C-Lens and TRP leads to a rigid length of about ~ 5 mm. A large rigid length and diameter of catheter tip will increase the risk and difficulty of intervention, especially for some tortuous, small arteries. Therefore, a further research on how to shorten the rigid length of HR-IVPA endoscope deserves to be developed.

The clinical catheter is disposable product and cross use will never happen. The advantage of HR-IVPA endoscope in IVPA imaging was demonstrated by the single imaging experiments

of tungsten wires, imitated stent and lipid. The intention of multiple day-trace use described in section 3.1 is to further verify the robustness of HR-IVPA endoscope.

The optical design in this study aims to overcome the concerns on focus shift caused by optical dispersion. The beam waist was positioned at the expected focal length. Though a certain scattering of laser beam was caused by blood in the mixture. The diluted mixture may reduce the mie scattering to the laser beam with the long wavelength of 1200 and 1720 nm. Hence, the imaging experiments were conducted smoothly in the mixture, close to clinical setting, and the imaging result demonstrated the high-robustness characteristic of HR-IVPA endoscope. A further simulation on the transmitting and scattering of laser beam in blood and tissue may have to use Monte Carlo analysis, which deserves our deep exploration in future work

Based on the study of the optical path structure in Fig. 2, with an equal distance L , the long-wavelength laser is focused with a long depth of focus and a large waist size, and the short-wavelength laser is focused with a relatively short focus depth and a relatively small waist size. Considering the scattering of light in biological tissues and the depth distribution of lipid plaques, the long-wavelength laser with low numerical aperture is suitable for deep-penetration IVPA imaging of lipid-rich plaque, and the short-wavelength laser with high numerical aperture is suitable for optical-resolution IVPA imaging of near-field stent issues. Hence, Multispectral IVPA imaging may be a favorable tool for the studies of cardiovascular disease, such as restenosis in the stent, positive and negative remodeling of artery, etc.

5. Conclusion

In summary, a high-robustness intravascular photoacoustic (HR-IVPA) endoscope was developed and tested. The optical path structure of the endoscope, overcoming the ambiguous focus shift caused by chromatic dispersion, acquired a well-founded light-resolution focus under experimental conditions. The HR-IVPA endoscope features an improved optical coupling of about ~90% and a cut-off free damage threshold. In addition, reconstructed PA images of stent, lipid, and tungsten wires at different depth were obtained *ex vivo* to verify the robustness and imaging ability of the endoscope. This study shows that the HR-IVPA endoscope can provide higher SNR and transverse resolution for repeatable imaging and supports great potential for clinical applications in intravascular plaque and stent imaging.

Funding

National Natural Science Foundation of China (61822505, 11774101, 61627827); China Postdoctoral Science Foundation (2019M652943); Natural Science Foundation of Guangdong Province (2019A1515011399); Guangzhou Science and Technology Program key projects (2019050001).

Disclosures

The authors declare no conflicts of interest.

References

1. B. Cannon, "Cardiovascular disease: biochemistry to behaviour," *Nature* **493**(7434), S2–S3 (2013).
2. C. L. de Korte, M. J. Sierevogel, F. Mastik, C. Strijder, J. A. Schaar, E. Velema, G. Pasterkamp, P. W. Serruys, and A. F. W. van der Steen, "Identification of atherosclerotic plaque components with intravascular ultrasound elastography *in vivo*: a yucatan pig study," *Circulation* **105**(14), 1627–1630 (2002).
3. R. Liu, Y. Zhang, Y. Zheng, Y. Liu, Y. Zhao, and L. Yi, "Automated detection of vulnerable plaque for intravascular optical coherence tomography images," *Cardiovasc. Eng. Technol.* **10**(4), 590–603 (2019).
4. B. E. Bouma, "Evaluation of intracoronary stenting by intravascular optical coherence tomography," *Heart* **89**(3), 317–320 (2003).
5. Y. Tan, K. Xia, Q. Ren, and C. Li, "Three-dimensional photoacoustic imaging via scanning a one dimensional linear unfocused ultrasound array," *Opt. Express* **25**(7), 8022–8028 (2017).

6. M. Yang, L. Zhao, X. He, N. Su, C. Zhao, H. Tang, and C. Li, "Photoacoustic/ultrasound dual imaging of human thyroid cancers: an initial clinical study," *Biomed. Opt. Express* **8**(7), 3449–3457 (2017).
7. S. Iskander-Rizk, M. Wu, G. Springeling, F. Mastik, R. H. Beurskens, A. F. van der Steen, and G. van Soest, "Catheter design optimization for practical intravascular photoacoustic imaging (IVPA) of vulnerable plaques," *Proc. SPIE* **10471**, 1047111 (2018).
8. R. Puri, M. I. Worthley, and S. J. Nicholls, "Intravascular imaging of vulnerable coronary plaque: current and future concepts," *Nat. Rev. Cardiol.* **8**(3), 131–139 (2011).
9. W. Wei, X. Li, Q. Zhou, K. K. Shung, and Z. Chen, "Integrated ultrasound and photoacoustic probe for coregistered intravascular imaging," *J. Biomed. Opt.* **16**(10), 106001 (2011).
10. M. Wu, G. Springeling, M. Lovrak, F. Mastik, S. Iskander-Rizk, T. Wang, H. M. van Beusekom, A. F. van der Steen, and G. Van Soest, "Real-time volumetric lipid imaging *in vivo* by intravascular photoacoustics at 20 frames per second," *Biomed. Opt. Express* **8**(2), 943–953 (2017).
11. B. Y. Hsieh, S. L. Chen, L. J. Guo, and P. C. Li, "Integrated intravascular ultrasound and photoacoustic imaging scan head," *Opt. Lett.* **35**(17), 2892–2894 (2010).
12. W. Wei, X. Li, Q. Zhou, K. K. Shung, and Z. Chen, "Integrated ultrasound and photoacoustic probe for co-registered intravascular imaging," *J. Biomed. Opt.* **16**(10), 106001 (2011).
13. X. Ji, K. Xiong, S. Yang, and D. Xing, "Intravascular confocal photoacoustic endoscope with dual-element ultrasonic transducer," *Opt. Express* **23**(7), 9130–9136 (2015).
14. J. Zhang, S. Yang, X. Ji, Q. Zhou, and D. Xing, "Characterization of lipid-rich aortic plaques by intravascular photoacoustic tomography: *ex vivo* and *in vivo* validation in a rabbit atherosclerosis model with histologic correlation," *J. Am. Coll. Cardiol.* **64**(4), 385–390 (2014).
15. Z. Chen, S. Yang, and D. Xing, "*In vivo* detection of hemoglobin oxygen saturation and carboxyhemoglobin saturation with multiwavelength photoacoustic microscopy," *Opt. Lett.* **37**(16), 3414–3416 (2012).
16. K. Jansen, A. F. van der Steen, H. M. van Beusekom, J. W. Oosterhuis, and G. van Soest, "Intravascular photoacoustic imaging of human coronary atherosclerosis," *Opt. Lett.* **36**(5), 597–599 (2011).
17. M. Xu, P. Lei, J. Feng, F. Liu, S. Yang, and P. Zhang, "Photoacoustic characteristics of lipid-rich plaques under ultra-low temperature and formaldehyde treatment," *Chin. Opt. Lett.* **16**(3), 031702 (2018).
18. K. Jansen, A. F. van der Steen, H. M. van Beusekom, J. W. Oosterhuis, and G. van Soest, "Intravascular photoacoustic imaging of human coronary atherosclerosis," *Opt. Lett.* **36**(5), 597–599 (2011).
19. J. M. Yang, C. Favazza, R. Chen, J. Yao, X. Cai, K. Maslov, Q. Zhou, K. K. Shung, and L. V. Wang, "Simultaneous functional photoacoustic and ultrasonic endoscopy of internal organs *in vivo*," *Nat. Med.* **18**(8), 1297–1302 (2012).
20. H. Guo, C. Song, H. Xie, and L. Xi, "Photoacoustic endomicroscopy based on a MEMS scanning mirror," *Opt. Lett.* **42**(22), 4615–4618 (2017).
21. H. Guo, W. Qi, M. He, J. Rong, and L. Xi, "Co-registered photoacoustic and ultrasound imaging for tongue cancer detection," *J. Innov. Opt. Health Sci.* **11**(03), 1850008 (2018).
22. Y. Yuan, S. Yang, and D. Xing, "Preclinical photoacoustic imaging endoscope based on acousto-optic coaxial system using ring transducer array," *Opt. Lett.* **35**(13), 2266–2268 (2010).
23. B. Wang, J. L. Su, J. Amirian, S. H. Litovsky, R. Smalling, and S. Emelianov, "Detection of lipid in atherosclerotic vessels using ultrasound-guided spectroscopic intravascular photoacoustic imaging," *Opt. Express* **18**(5), 4889–4897 (2010).
24. K. Jansen, M. Wu, A. F. W. van der Steen, and S. G. Van, "Lipid detection in atherosclerotic human coronaries by spectroscopic intravascular photoacoustic imaging," *Opt. Express* **21**(18), 21472 (2013).
25. J. Hui, Q. Yu, T. Ma, P. Wang, Y. Cao, R. S. Bruning, Y. Qu, Z. Chen, Q. Zhou, M. Sturek, J. X. Cheng, and W. Chen, "High-speed intravascular photoacoustic imaging at 1.7 μm with a KTP-based OPO," *Biomed. Opt. Express* **6**(11), 4557–4566 (2015).
26. T. J. Allen, A. Hall, A. P. Dhillon, J. S. Owen, and P. C. Beard, "Spectroscopic photoacoustic imaging of lipid-rich plaques in the human aorta in the 740 to 1400 nm wavelength range," *J. Biomed. Opt.* **17**(6), 061209 (2012).
27. A. B. Karpouk, B. Wang, and S. Y. Emelianov, "Development of a catheter for combined intravascular ultrasound and photoacoustic imaging," *Rev. Sci. Instrum.* **81**(1), 014901 (2010).
28. X. Li, W. Wei, Q. Zhou, K. K. Shung, and Z. Chen, "Intravascular photoacoustic imaging at 35 and 80 MHz," *J. Biomed. Opt.* **17**(10), 1060051 (2012).
29. Y. Cao, J. Hui, A. Kole, P. Wang, Q. Yu, W. Chen, M. Sturek, and J. Cheng, "High-sensitivity intravascular photoacoustic imaging of lipid-laden plaque with a collinear catheter design," *Sci. Rep.* **6**(1), 25236 (2016).
30. X. Bai, X. Gong, W. Hau, R. Lin, J. Zheng, and C. Liu, "Intravascular Optical-Resolution Photoacoustic Tomography with a 1.1 mm Diameter Catheter," *PLoS One* **9**(3), e92463 (2014).
31. Y. Li, X. Gong, C. Liu, R. Lin, W. Hau, X. Bai, and L. Song, "High-speed intravascular spectroscopic photoacoustic imaging at 1000 A-lines per second with a 0.9-mm diameter catheter," *J. Biomed. Opt.* **20**(6), 065006 (2015).
32. L. Wang, P. Lei, X. Wen, P. Zhang, and S. Yang, "Tapered fiber-based intravascular photoacoustic endoscopy for high-resolution and deep-penetration imaging of lipid-rich plaque," *Opt. Express* **27**(9), 12832–12840 (2019).
33. K. Song, I. Kim, S. Bang, J. Y. Jung, and Y. Nam, "Corrosion resistance of water repellent aluminum surfaces with various wetting morphologies," *Appl. Surf. Sci.* **467-468**, 1046–1052 (2019).
34. <https://www.bostonscientific.com/en-US/products/fr-ivus-systems/complex-pci-ivus-catheter.html>

35. <https://www.epotek.com/site/component/products/products.html?cat=3&title=Optical%20Products&search=0&sign=0&value=>
36. Laser Institute of America, *American National Standard for Safe Use of Lasers ANSI Z136.1–2014* (American National Standards Institute, Inc., 2014).
37. A. M. Ghodgaonkar and R. D. Tewari, "Measurement of apex angle of the prism using total internal reflection," *Opt. Laser Technol.* **36**(8), 617–624 (2004).
38. S. Wakelin and C. R. Bagshaw, "A prism combination for near isotropic fluorescence excitation by total internal reflection," *J. Microsc.* **209**(2), 143–148 (2003).